Influence of Pr-doping on structural, electronic transport, magnetic properties of perovskite molybdates Sr$_{1-x}$Pr$_x$MoO$_3$ ($0 \leq x \leq 0.15$)

S.B. Zhang, Y.P. Sun *, B.C. Zhao, X.B. Zhu, W.H. Song

Key Laboratory of Materials Physics, Institute of Solid State Physics, Chinese Academy of Sciences, Hefei 230031, People's Republic of China

Abstract

The effect of Pr-doping on structural, electronic transport, magnetic properties in perovskite molybdates Sr$_{1-x}$Pr$_x$MoO$_3$ ($0 \leq x \leq 0.15$) has been investigated. The Pr-doping at Sr-site does not change the space group of the samples, but decreases the lattice parameter a. The magnitude of resistivity ρ increases initially ($x \leq 0.08$) and then decreases with further increasing Pr-doping level x and $\rho(T)$ behaves as T^2 and T dependence in the low-temperature range blow T^* and high-temperature range of 150 K $< T <$ 350 K, related to the electron–electron (e–e) and electron–phonon (e–ph) scattering, respectively. The magnetic susceptibility χ value of the sample increases with increasing x and the $\chi(T)$ curve for all samples can be well described by the model of exchange-enhanced paramagnetism. The specific heat magnitude in the low-temperature region increases with increasing Pr-doping level. The specific heat value agrees with the classical Dulong–Petit phonon specific heat, $C_{cl} = 3k_B r N_A =$ 124.7 J/mol K in the high-temperature region and the temperature dependence of the specific heat can be well described by the formula $C_p(T)/T = \gamma_e + \beta_p T^2$ in the low-temperature range. These behaviors can be explained by the competition between the increase in the density of state (DOS) at Fermi energy level and the disorder effect due to Pr-doping.
© 2006 Elsevier Ltd. All rights reserved.

1. Introduction

Transition-metal oxide (TMO) systems have attracted much attention for a long time because of their importance in both fundamental issues in condensed-matter physics and the potential for applications. The discovery of high-transition temperature (T_c) superconductivity in cuprates and colossal magnetoresistance (CMR) effect in manganites has given extensive researches in 3d TMO system. Compared with 3d TMO system, much less has been known about the properties in 4d TMO except for Ru-based oxides. The 4d TMO are characterized by more extended orbits than those in the 3d TMO system. So, they have unique electronic structure. It has been generally believed that the electrons in these orbits feel rather weak on-site Coulomb repulsion energy and the 4d orbits hybridize more strongly with their neighbouring orbits (e.g. O^{-2} 2p) than the 3d ones. Therefore, 4d TMO have numerous

intriguing properties such as superconductivity (SC) [1], metal–insulator (M–I) transition [2], pesudogap formation [3,4] and non-Fermi liquid behavior [5,6], etc. These properties are characteristic of strongly correlated electron systems like 3d TMO, which have rather localized electron orbits and electrons feel strong Coulomb repulsion from each other [7,8].

Among the 4d transition elements Mo is a unique one. Its perovskite compounds SrMoO$_3$ and Sr$_2$MoO$_4$ have been studied in the past. SrMoO$_3$ exhibits metallic-like conductivity in a very broad temperature region with Pauli paramagnetism [9,10]. And high conductivity is the interesting property for people. Wang et al. [11] reported the growth of the polycrystalline thin-film samples of SrMoO$_3$ on SrTiO$_3$ substrates by pulsed laser deposition. The resistivity data of the samples show metallic behavior with $\rho(300 \text{ K}) = \sim 100 \ \mu\Omega$ cm. And the single crystals of SrMoO$_3$ obtained by Nagai et al. [12] reveal quite low resistivity at 300 K ($\rho(300 \text{ K}) = 5.1 \ \mu\Omega$ cm), which is the lowest to date in the values of $\rho(300 \text{ K})$ of all the oxides. Thus SrMoO$_3$ may be a very good oxide material for electrodes and interconnects. In developing process of conductive oxides, isotropic conductivity is preferable to anisotropic one because the high

---

conductivity can be expected in a polycrystalline form with random orientations of grains. Therefore, (pseudo) cubic metallic oxides, which show low resistivity and consist of low-cost elements, are in great demand from the application side. Because the structure of $SrMoO_3$ is simple cubic perovskite, so the three-dimensional electrical conductivity can be expected. Compared to the high cost of Re and Pd hindering the application of ReO_3 [13] and $PdCoO_2$ [14], Mo is preferred to Re and Pd because its lower raw material cost. These features make $SrMoO_3$ a candidate for oxide electrodes and/or interconnects material for large-scale integrated circuit (LSI) chips and ferroelectric random access memory (FRAM). Can the conductivity be enhanced or not if we dope higher valence ions on Sr or Mo site? And how do the other physical properties vary? However, few study as to the doping effect at Sr or Mo site of $SrMoO_3$ has been performed so far. In this paper we systematically investigated the effect of Pr-doping at Sr-site on structural, magnetic, electronic transport and specific heat properties in the chemically prepared polycrystalline sample $SrMoO_3$.

2. Experimental

Polycrystalline samples of $Sr_{1-x}Pr_xMoO_4$ ($0 \le x \le 0.15$) were prepared by a citrate gel technique [15,16]. Stoichiometric amounts of high purity $Sr(NO_3)_2$ and $(NH_4)_6Mo_7O_{24} \cdot 4\text{-}H_2O$ were dissolved, respectively, in the distilled water. In order to avoid the error induced by the serious hydrophilic property of the praseodymium nitrate, we dissolved Pr_2O_3 powder in the nitric acid to get $Pr(NO_3)_3$ solution. An excess of citric acid (1.5 mol citric acid/mol M, M = Sr, Pr, Mo) is then added to each solution. The obtained solutions are mixed together by beater for more than 2 h and the final solution is put into a rotary evaporator until the formation of a viscous liquid, which is then heated at 353 K for more than 48 h in a resistive heater. Once a powder has been obtained, the catalyst precursor is pre-calcined at 573 K for 24 h in order to allow the decomposition of the citrate ion involving the formation of CO_2 and H_2O. After the pre-calcination treatment, the catalyst precursor was calcined at 773, 873 and 1373 K for 24 h, respectively, with three intermediate grinding. Then the yellowy compounds $Sr_{1-x}Pr_xMoO_4$ can be obtained. The compounds were ground and pressed into small pellets about 10 mm diameter and 2 mm thickness. These pellets were reduced in a H_2/Ar (5%:95%) flow at 1173 K for 12 h, then we can get the deep red colored products of $Sr_{1-x}Pr_xMoO_3$.

X-ray powder diffraction pattern was collected using a Philips X' pert PRO X-ray diffractometer with Cu K_α radiation at room temperature. The magnetic measurements were carried out with a commercial superconducting quantum interference device (SQUID) system (Quantum Design MPMS) ($1.8\ \text{K} \le T \le 400\ \text{K}$, $0\ \text{T} \le H \le 5\ \text{T}$). The resistance was measured by a standard four-probe technique and the specific heat was measured in a commercial physical property measurement system (Quantum Design PPMS) ($1.8\ \text{K} \le T \le 400\ \text{K}$, $0\ \text{T} \le H \le 9\ \text{T}$).

3. Results and discussion

Fig. 1 shows X-ray diffraction (XRD) patterns of $Sr_{1-x}Pr_xMoO_3$ ($x = 0$, 0.02, 0.05, 0.08, 0.1 and 0.15) samples. The powder X-ray diffraction at room temperature shows that all the samples are single-phase with no detectable secondary phase. XRD patterns of all samples can be indexed by a cubic lattice with space group $Pm3m$. The lattice parameters are refined by the standard Rietveld technique [17] and the fitting between the experimental spectra and calculated values is relatively good based on the consideration of lower R_p, R_{wp} and χ^2 values as shown in Table 1. And we have shown the experimental and calculated XRD patterns for the sample $x = 0.15$ in Fig. 2. The inset of Fig. 2 gives the variation of the obtained lattice parameter a (Å) with x (%). Obviously, the lattice parameter a decreases with increasing Pr-doping level x. It is known that the ionic radius of Pr^{3+} ion (1.179 Å) is smaller than that of Sr^{2+} ion (1.44 Å). So the lattice parameter of the sample decreases when the Sr^{2+} ions are partially substituted by Pr^{3+} ions.

The temperature dependence of resistivity $\rho(T)$ for $Sr_{1-x}Pr_xMoO_3$ ($0.02 \le x \le 0.15$) samples at zero field is shown in Fig. 3 in the temperature range of 5–350 K. The resistivity of all samples shows a metallic behavior ($d\rho/dT > 0$) in the whole temperature range studied. It is found that the value of ρ increases with increasing Pr-doping level, but as $x \ge 0.10$, ρ decrease with increasing Pr-doping content. The metallic-like conductivity of $SrMoO_3$ is related to the delocalized $4d^2$ electrons of Mo^{4+} cations which act as the carriers in this material [18]. That was already verified by X-ray photoelectron spectroscopy (XPS) measurement [8]. In the Pr-doped $Sr_xPr_{1-x}MoO_3$ samples, when partial Sr^{2+} were replaced by Pr^{3+} ions, correspondingly, some Mo^{4+} ions should be reduced to Mo^{3+} ions in order to keep the balance of the valence in one formula. So the electron numbers in t_{2g} orbits will add to three, finally lead to the increase in the amount of delocalized electrons for conductivity in these Pr-doped samples. That is to say, the density of states (DOS) at Fermi energy level will increase which can be confirmed by the increase in the electronic specific-heat coefficient γ_e (see below). However,
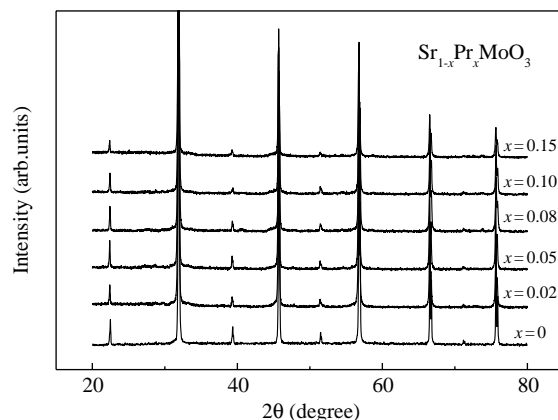

Fig. 1. The X-ray diffraction patterns of the samples $Sr_{1-x}Pr_xMoO_3$ ($x = 0.02$, 0.05, 0.08, 0.10, 0.15).

Table 1
Structural and electronic transport parameters of $Sr_{1-x}La_xMoO_3$ samples

x	$x=0.02$	$x=0.05$	$x=0.08$	$x=0.10$	$x=0.15$
R_p (%)	8.392	8.767	8.564	8.458	8.393
R_{wp}	10.680	11.763	11.078	11.024	10.931
χ^2	2.574	3.028	2.890	2.829	2.791
ρ_0 (mΩ cm)	0.15(2)	0.28(3)	0.55(8)	0.49(9)	0.41(2)
A_1 ($\mu\Omega$ cm/K^2)	$9.3(3)\times10^{-3}$	$2.45(5)\times10^{-2}$	$4.06(1)\times10^{-2}$	$3.24(1)\times10^{-2}$	$1.99(3)\times10^{-2}$
A_2 ($\mu\Omega$ cm/K)	0.30(3)	1.30(1)	4.19(9)	6.12(5)	1.23(2)
RRR ($\rho_{300\ K}/\rho_{5\ K}$)	5.0	6.0	5.2	4.1	3.9
T^* (K)	137	125	106	138	120

the Pr-doping also introduces a disorder effect in the sample. Consequently, there exist two competing components in the Pr-doped samples, which lead to the complex electronic transport behavior. Namely, in low-temperature region the disorder effect is mainly responsible for the change of resistivity, while the effect of an increase in the DOS at Fermi energy level is more prominent in high temperature region.

In order to further understand transport properties, we fit the $\rho(T)$ data of all samples for different temperature ranges using a formula $\rho(T)=\rho_0+AT^p$, where ρ_0, A and p are the residual resistivity, coefficient for T^p term and temperature exponent, respectively. The inset of Fig. 3 shows the plot of ρ versus T^2 for the sample with $x=0.02$. In the low-temperature region below T^*, the resistivity is well described with $\rho(T)=\rho_0+A_1T^2$, which indicates that the temperature dependence of the resistivity is dominated by electron–electron (e–e) scatting. T^* values for all samples are listed in Table 1. And the obtained coefficient A_1 is also denoted in Table 1. The temperature independent term ρ_0 in the $\rho(T)$ relation can be ascribed to the scattering process such as impurities, defects, grain boundaries, and domain walls scattering, which could not be detected by X-ray diffraction. We also figure out the value of the residual resistivity ratio (defined as RRR$=\rho_{300\ K}/\rho_{5\ K}$) as follows: 4.9, 6.0, 5.2, 4.1 and 3.9 for $x=0.02$, 0.05, 0.08, 0.10 and 0.15, respectively. In the high-temperature region of 150 K$< T<$ 350 K, the $\rho(T)$ curves for all samples are described by a nearly straight line with $p\sim1$, implying that the electron–phonon (e–ph) scattering mechanism dominates the electronic transport behavior in this temperature region. The fitting parameter A_2 for linear term is also shown in Table 1. The temperature dependence of resistivity at an applied field of 5 T is also measured (not shown here), no detectable magnetoresistance (MR) is observed.

The temperature dependence of magnetic susceptibility $\chi(T)=M/H$ for all samples is shown in Fig. 4 between 5 and 350 K. As it can be seen that the magnetic susceptibility $\chi(T)$ decreases with increasing temperatures in the high-temperature region. So the magnetic properties of the samples can not be completely described with Pauli paramagnetism. And the value of the magnetic susceptibility $\chi(T)$ is about one order of magnitude bigger than the pure $SrMoO_3$ [1]. No hysteresis is observed in the curve of magnetization versus applied magnetic field $M(H)$. Hence, long-range ferromagnetic (FM) order does not exist in these samples. Moreover, a very weak magnetic response to the external magnetic field as shown in

Fig. 5(a) also indicates no long-range (FM) order in the typical sample $Sr_{0.98}Pr_{0.02}MoO_3$. That indeed the case which is made abundantly clear by the Arrott plots as shown in Fig. 5(b), as elucidated below. In Fig. 5(b), it is can be seen that a linear extrapolation of the high-field portions of $M^2-(H/M)$ isotherms to $H=0$ yields no positive intercept on the M^2 axis for the sample indicating thereby that no spontaneous magnetization exits at $T=5$ K. And the concave downward curvature at low fields in the $M(H_{ext})$ isotherm taken at 5 K on the sample $Sr_{0.98}Pr_{0.02}MoO_3$ is the characteristic of exchange-
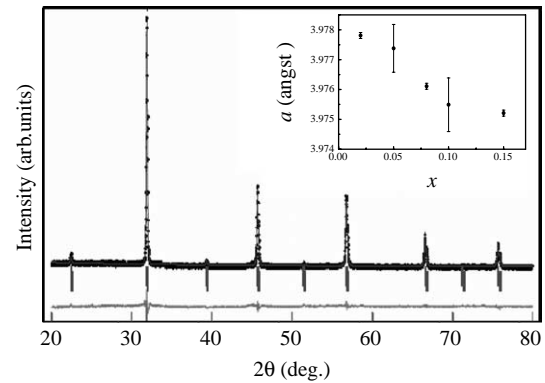

Fig. 2. XRD patterns of the sample $Sr_{0.85}Pr_{0.15}MoO_3$. Crosses indicate the experimental data and the calculated data is the continuous line overlapping them. The lowest curve shows the difference between experimental and calculated patterns. The vertical bars indicate the expected reflection positions. The inset is the variation of the lattice parameter a (Å) with x.
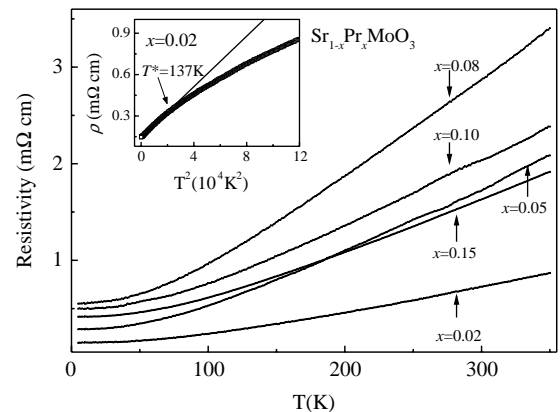

Fig. 3. The temperature dependence of the resistivity for $Sr_{1-x}Pr_xMoO_3$ ($x=$ 0.02, 0.05, 0.08, 0.1, 0.15) samples at zero field. Inset shows the plot of ρ versus T^2 for the sample with $x=0.02$.
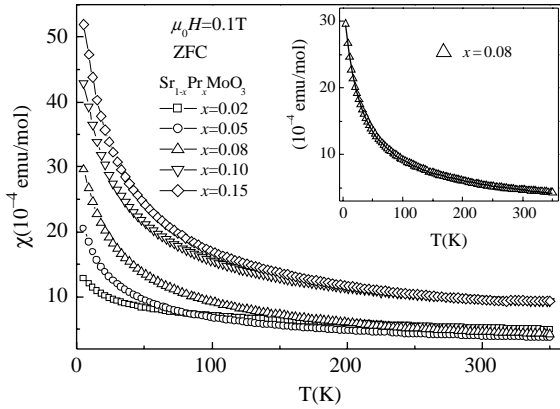
Fig. 4. The temperature dependence of DC magnetic susceptibility for the $Sr_{1-x}Pr_xMoO_3$ (x=0.02, 0.05, 0.08, 0.1, 0.15) samples measured at an applied magnetic field of 0.1 T. The inset shows the fitting result in whole temperature region for the sample with x=0.08 and the line is the calculated curve.
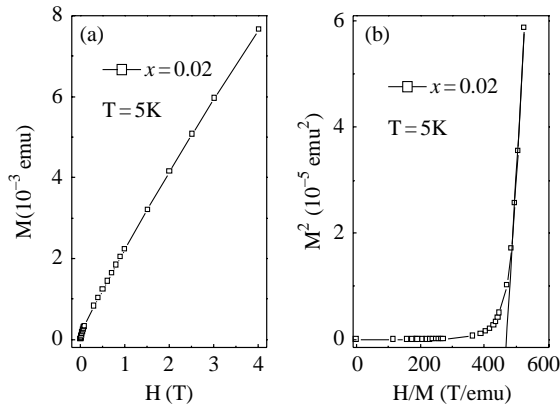

Fig. 5. (a) Magnetization versus magnetic field at 5 K for the sample $Sr_{0.98}Pr_{0.02}MoO_3$; (b) $[M(T,H)]^2$ versus $H/M(T,H)$ converted from (a).

enhanced paramagnetism [19]. It is known that the outer-shell electrons distribution of Pr^{3+} ion is $4f^2$ with S=1. As one Sr^{2+} ion is replaced by Pr^{3+} ion, one Mo^{3+} ion (with $4d^3$ electronic configuration) is introduced to keep the sample electronic neutrality. Thus the Pr-doping at Sr-site will give rise to the increase in carrier number. This may be the reason that the Pr-doped sample has a big magnetic susceptibility $\chi(T)$ value and the magnetic property of the Pr-doped sample can be described by an exchange-enhanced paramagnetism model. In view

of the Curie–Weiss form of $\chi(T)$ data taken on the samples $Sr_{1-x}Pr_xMoO_3$ ($0 \leq x \leq 0.15$) have been fitted to the following expression in whole temperature range [19]

$$\chi(T) = \chi_{CW}(T) + \chi_{EP}(T) = C/(T - \Theta) + \chi_{EP}(0)(1 - A_3 T^2)$$

where χ_{CW} and χ_{EP} are the Curie–Weiss (C–W) and exchange-enhanced Pauli (EP) contributions to susceptibility, respectively, C is the Curie constant, Θ is the paramagnetic Curie temperature,

$$A_3 = \frac{\pi^2 k_B^2}{6} \left\{ \left[\frac{N'(E_F)}{N(E_F)} \right]^2 - \left[\frac{N''(E_F)}{N(E_F)} \right] \right\}$$

$N(E_F)$ is the density of states (DOS) at the Fermi energy level, E_F, per atom $N'(E_F)$ and $N''(E_F)$ are its first and second energy derivatives. The values of the fitting parameters C, Θ, $\chi_{EP}(0)$ and A_3 obtained are shown in Table 2. It indicates that negative Θ reflects antiferromagnetic (AFM) interaction between the spins on the Pr-ions and magnetic impurity atoms that occupy the nearest-neighbor lattice sites.

Using the Curie constant C obtained by fitting the data, we can get the molar effective magnetic moment μ_{eff} (μ_B) of all samples. The molar effective magnetic moment (per mole of formula unit) can be calculated by the following equation [20]:

$$\mu_{eff}^{exp} = 2.83 \left[\frac{C}{\eta} \right]^{1/2} \mu_B,$$

where η is the number of atoms in one single cell. Because the electrons in t_{2g} orbits of Mo ions are itinerant, there only Pr^{3+} ions have contribution for the effective magnetic moment. As a result, we also calculated the effective magnetic moment in theory using an equation:

$$\mu_{eff}^{theo} = g\sqrt{S(S+1)x},$$

where g is the Lande factor, S is the spin quantum number of magnetic ions, and the x is the stoichiometry proportion in one formula. Both theoretical (μ_{eff}^{theo}) and experiment (μ_{eff}^{exp}) values are listed in Table 2. It indicates that μ_{eff}^{theo} is almost consistent with μ_{eff}^{exp}. So the delocalization of all the 4d electrons of Mo^{4+} and Mo^{3+} ions has also been proved by this.

Fig. 6 shows the temperature dependence of specific heat C_p at zero magnetic field in the temperature range of 5–300 K except for the sample $Sr_{0.85}Pr_{0.15}MoO_3$ in a temperature range

Table 2
Magnetic and specific heat parameters of $Sr_{1-x}La_xMoO_3$ samples

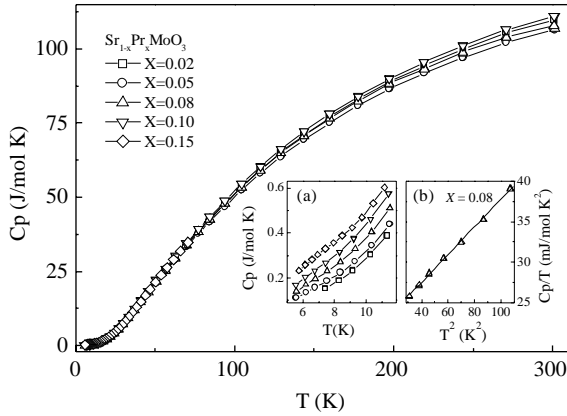| x	x=0.02	x=0.05	x=0.08	x=0.10	x=0.15
C (emu K/mol)	0.023(4)	0.048(4)	0.084(8)	0.112(9)	0.140(1)
Θ (K)	−25.88	−22.33	−26.12	−25.84	−25.23
$\chi_{EP}(0)$ (10^{-4} emu/mol)	5.3(3)	2.8(3)	2.6(5)	6.6(6)	5.7(1)
A_3 (10^{-6}/K^2)	1.635	1.383	2.130	0.620	0.739
γ_e (mJ/K^2 mol)	10.67	15.35	20.73	26.39	37.38
β_p (mJ/mol K^4)	0.1780	0.1640	0.1702	0.1726	0.1139
K–W ratio ($\mu\Omega$ cm (K mol/mJ)^2)	8.15×10^{-5}	10.4×10^{-5}	9.45×10^{-5}	4.65×10^{-5}	1.42×10^{-5}
μ_{eff}^{exp} (μ_B)	0.43	0.62	0.82	0.94	1.05
μ_{eff}^{theo} (μ_B)	0.40	0.63	0.80	0.89	1.10

Fig. 6. Specific heat as a function of temperature for $Sr_{1-x}Pr_xMoO_3$ ($x=0.02$, 0.05, 0.08, 0.1, 0.15) samples. The inset (a) is a magnified plot of $C_p(T)$ behavior in the low-temperature region ($T<12$ K). And the inset (b) shows the fitting result in low-temperature range below 10 K for the sample with $x=0.08$.

of 5–70 K. Considering the only one magnetic Mo^{4+} ion in a single cell, we express C_p in 1-mol formula unit. As we can see all the samples show metallic $C_p(T)$ behavior and the C_p value increases with increasing Pr-doping level, which can be clearly seen in a magnified plot of $C_p(T)$ in low-temperature region of $T<12$ K as shown in the inset (a) of Fig. 6. In addition, $C_p(T)$ has a trend to converge to a constant value in the high-temperature region, which agrees with the classical Dulong–Petit phonon specific heat. We can calculate it by $C_{cl}=3k_BrN_A=124.7$ J/mol K [21], where $r=5$ is the number of atoms in one formula unit and N_A is the Avogadro's number. In the low temperature region of $T\leq10$ K, the C_p/T versus T^2 data can be well fitted by the formula $C_p(T)/T=\gamma_e+\beta_pT^2$, a typical fitting result for the sample with $x=0.08$ is plotted in the inset (b) of Fig. 6. The obtained electronic specific-heat coefficient γ_e and the specific heat coefficient of phonon β_p are shown in Table 2. As it can be seen, the γ_e increases with increasing Pr-doping level, while the β_p does not show a clear regular variation. The increase in γ_e implies the increase in the DOS at Fermi energy level due to the partial substitution of Pr^{3+} for Sr^{2+} ions. It is easy to comprehend based on the reduced valence of partial Mo^{4+} ions to Mo^{3+} ions due to the electron-doping, which results in the increase in the electron number in Mo-ion's t_{2g} orbits. In other words, the number of itinerant electrons for conductivity increases due to Pr-doping at Sr-site. Based on the fitting parameter β_p, Debye temperature Θ_D: 222, 228, 225, 224, 257 K for the samples with $x=0.02$, 0.05, 0.08, 0.10, 0.15, respectively, can be obtained using the following equation [22]:

$$\Theta_D=\left(\frac{12\pi^4pR}{5\beta_p}\right)^{1/3}$$

where R is the gas constant and p is the number of atoms in each molecule.

In order to get the information about electron correlation in studied samples, the Kadowaki–Woods (K–W) ratio is calculated. The K–W ratio, defined as A/γ_e^2, which becomes a universal value $a_0=1.0\times10^{-5}$ $\mu\Omega$ cm(K mol/mJ)^2 in most

strongly-correlated electron systems [23]. The calculated results for all the doped samples are shown in Table 2. It indicates that the e–e correlation of the doped samples became stronger with increasing Pr-doping level as a whole.

4. Conclusions

In summary, Pr-doped perovskite-stuctural molybdates $Sr_{1-x}Pr_xMoO_3$ ($0\leq x\leq0.15$) have been prepared by citrate gel method. The structural, electronic transport, magnetic properties have been investigated. The partial substitution of Pr^{3+} for Sr^{2+} ions does not change the space group of the samples, but decreases the lattice parameter a. The temperature dependence of resistivity $\rho(T)$ behaves as T^2 and T dependence in the low temperature range blow T^* and high-temperature range of 150 K $<T<$ 350 K, respectively, which is suggested to originate from the e–e and e–ph scattering. The resultant electronic transport variation due to Pr-doping is attributed to the combined effect of the increase in DOS at Fermi energy level and the introduction of disorder effect. The localized f electrons of Pr^{3+} which contribute to the C–W part make pr-doped samples have a bigger magnetic susceptibility $\chi(T)$ value than free doped sample. At the same time, itinerant electrons of Mo^{3+} and Mo^{4+} ions make the EP contribution to susceptibility. The interaction between them results in the appearance of the exchange-enhanced paramagnetic $\chi(T)$ for all Pr-doped samples.

References

[1] K. Ishida, H. Mukuda, Y. Kitaoka, K. Asayama, Z.Q. Mao, Y. Mori, Y. Macno, Nature (London) 396 (1998) 658.
[2] J.S. Lee, Y.S. Lee, T.W. Noh, K. Char, J. Park, S.-J. Oh, J.-H. Park, C.B. Eom, T. Takeda, R. Kanno, Phys. Rev. B 64 (2001) 245107.
[3] Y.S. Lee, J.S. Lee, T.W. Noh, D.-Y. Byun, K.-S. Yoo, K. Yamaura, E. Takayama-Muromachi, Europhys. Lett. 55 (2001) 280.
[4] Y.S. Lee, J.S. Lee, K.W. Kim, T.W. Noh, Y. Jaejun, B. Yunkyu, M.K. Lee, B. Eom, Phys. Rev. B 64 (2001) 165109.
[5] P. Kostic, Y. Okada, N.C. Collins, Z. Schlesinger, J.W. Reiner, L. Klein, A. Kapitulnik, T.H. Geballe, M.R. Beasley, Phys. Rev. Lett. 81 (1998) 2498.
[6] J.S. Lee, Y. Jaejun, T.W. Noh, T.-H. Gimm, C. Han-Yong, C.B. Eom, Phys. Rev. B 66 (2002) 041104.
[7] I.C. Lekshmi, A. Gayen, M.S. Hegde, Mater. Res. Bull. 40 (2005) 93–104.
[8] I. Hase, I. Shin-Ichi, N. Shirakawa, J. Stalick, J. Low Temp. Phys. 131 (2003) 269–273.
[9] J.B. Goodenough, J.M. Longo, Landolt-Borstein Zahlenwerte und Funktionen, New Series BdIII/4a, vol. 255, 1970.
[10] U. Steiner, W. Reichelt, Z. Naturforsch 53b (1998) 110.
[11] H.H. Wang, D.F. Cui, Y.L. Zhou, Z.H. Chen, F. Chen, T. Zhao, H.B. Lu, G.Z. Yang, M.C. Xu, Y.C. Lan, X.L. Chen, H.J. Qian, Q. Liu, J. Cryst. Growth 261 (2001) 226.

[12] I. Nagai, N. Shirakawa, S.I. Ikeda, R. Iwasaki, H. Nishimura, M. Kosaka, Appl. Phys. Lett. 87 (2005) 024105.

[13] T.P. Pearsall, A. Lee, Phys. Rev. B 10 (1974) 2190.

[14] M. Tanaka, M. Hasegawa, H. Takei, J. Phys. Soc. Jpn. 65 (1996) 3973.

[15] M. Andrea, D. Michel, J. Solid State Chem. 177 (2004) 2339–2349.

[16] R. Agarmal, Z. Singh, V. Venugopal, J. Alloys Compd. 282 (1999) 231–235.

[17] L.B. McCusker, R.B. Von Dreele, D.E. Cox, D. Louër, P. Scandi, J. Appl. Cryst. 32 (1999) 35–36.

[18] J.B. Goodenough, J. Appl. Phys. 37 (1966) 1415.

[19] S.N. Kaul, A. Semwal, Phys. Rev. B 62 (2000) 13892.

[20] M.R. Lees, O. Petrenko, G. Balakrishnan, D.Mck. Paul, Phys. Rev. B 59 (1998) 1298.

[21] E.M. Levin, S.-S. Hou, S.L. Bud'ko, K. Schmidt-Rohr, J. Appl. Phys. 96 (2004) 5085.

[22] N. Shirakawa, K. Murata, H. Hashimoto, F. Iga, Y. Nishihara, J. Phys. Soc. Jpn. 66 (1997) 1405.

[23] S. Yonezawa, Y. Maeno, Phys. Rev. B 70 (2004) 184523.